Article

Site-specific reactivity of stepped Pt surfaces driven by stress release

Guangdong Liu[1,5], Arthur J. Shih[2,5], Huiqiu Deng[1], Kasinath Ojha[2], Xiaoting Chen[2], Mingchuan Luo[2], Ian T. McCrum[3], Marc T. M. Koper[2], Jeffrey Greeley[4✉] & Zhenhua Zeng[4✉]

Heterogeneous catalysts are widely used to promote chemical reactions. Although it is known that chemical reactions usually happen on catalyst surfaces, only specific surface sites have high catalytic activity. Thus, identifying active sites and maximizing their presence lies at the heart of catalysis research[1–4], in which the classic model is to categorize active sites in terms of distinct surface motifs, such as terraces and steps[1,5–10]. However, such a simple categorization often leads to orders of magnitude errors in catalyst activity predictions and qualitative uncertainties of active sites[7,8,11,12], thus limiting opportunities for catalyst design. Here, using stepped Pt(111) surfaces and the electrochemical oxygen reduction reaction (ORR) as examples, we demonstrate that the root cause of larger errors and uncertainties is a simplified categorization that overlooks atomic site-specific reactivity driven by surface stress release. Specifically, surface stress release at steps introduces inhomogeneous strain fields, with up to 5.5% compression, leading to distinct electronic structures and reactivity for terrace atoms with identical local coordination, and resulting in atomic site-specific enhancement of ORR activity. For the terrace atoms flanking both sides of the step edge, the enhancement is up to 50 times higher than that of the atoms in the middle of the terrace, which permits control of ORR reactivity by either varying terrace widths or controlling external stress. Thus, the discovery of the above synergy provides a new perspective for both fundamental understanding of catalytically active atomic sites and design principles of heterogeneous catalysts.

Cleavage of bulk metal to create surfaces, which leads to a reduction in the coordination of surface atoms and consequent charge redistribution, usually induces an attractive interaction between surface atoms. For Pt, the resulting tensile surface stress is about −5 N m^{-1} on (111) surface (refs. 13,14), which implies a surface pressure of over 2×10^5 atm on the surface atoms. This surface pressure, which is about 10% of the bulk modulus[14], provides a strong driving force for contraction of the surface. But this contraction is impossible on perfect Pt(111) because of the symmetry of the surface. However, as we demonstrate, the presence of even small imperfections, such as step-type defects, can break the symmetry and lead to release of the surface stress, relaxation of surface atoms and generation of inhomogeneous strain fields that may span multiple nanometres on transition metal surfaces (Fig. 1). The associated electronic and geometric effects lead to orders of magnitude differences in atomic site-specific catalytic activity, even for atoms with identical local environments (Fig. 2). This phenomenon provides a succinct explanation for the large errors that are often present in catalytic reactivity predictions based on discrete active-site models, resolves longstanding puzzles about the nature of the active site and structure sensitivity of the ORR in the literature, and enables a more accurate prediction and computational design of heterogeneous catalysts.

To demonstrate the existence of surface stress release due to step-like imperfections on single-crystal surfaces, as well as the dependence of the resulting surface strain on the step density, we constructed a series of stepped Pt(111) surfaces, consisting of steps separated by (111) terraces with widths ranging from around 1 nm to around 10 nm (Fig. 1b–f, Extended Data Figs. 1 and 2 and Extended Data Table 1). As shown in Fig. 1f,g, surface stress release and surface strain generation are induced on all such surfaces, with both stress release and strain increasing in magnitude with decreasing terrace width. For example, for Pt(21 21 20) with a terrace width of 10.1 nm, surface stress release and average surface strain are only 9% (0.42 N m^{-1}) and −0.7%, respectively. However, the corresponding values increase to 62% (3.0 N m^{-1}) and −4.7%, respectively, for Pt(221) with a terrace width of 0.8 nm.

Next, we demonstrate that the surface strain driven by surface stress release is highly inhomogeneous. As shown in Fig. 1b–e, atomic site-resolved strain can vary dramatically across terrace sites between steps, in spite of the fact that the terrace atoms all have the same local coordination numbers. In general, the maxima of atomic site-resolved strain are found on both sides of the step edges, where stress release is triggered, and the minima are located far from the step edges, in the middle of the terraces (Fig. 1b–e and Extended Data Fig. 3). For example, for Pt(21 21 20), the maximum strain and the minimum strain are

[1]Hunan Provincial Key Laboratory of High-Energy Scale Physics and Applications, School of Physics and Electronics, Hunan University, Changsha, China. [2]Leiden Institute of Chemistry, Leiden University, Leiden, The Netherlands. [3]Department of Chemical and Biomolecular Engineering, Clarkson University, Potsdam, NY, USA. [4]Davidson School of Chemical Engineering, Purdue University, West Lafayette, IN, USA. [5]These authors contributed equally: Guangdong Liu, Arthur J. Shih. ✉e-mail: jgreeley@purdue.edu; zeng46@purdue.edu
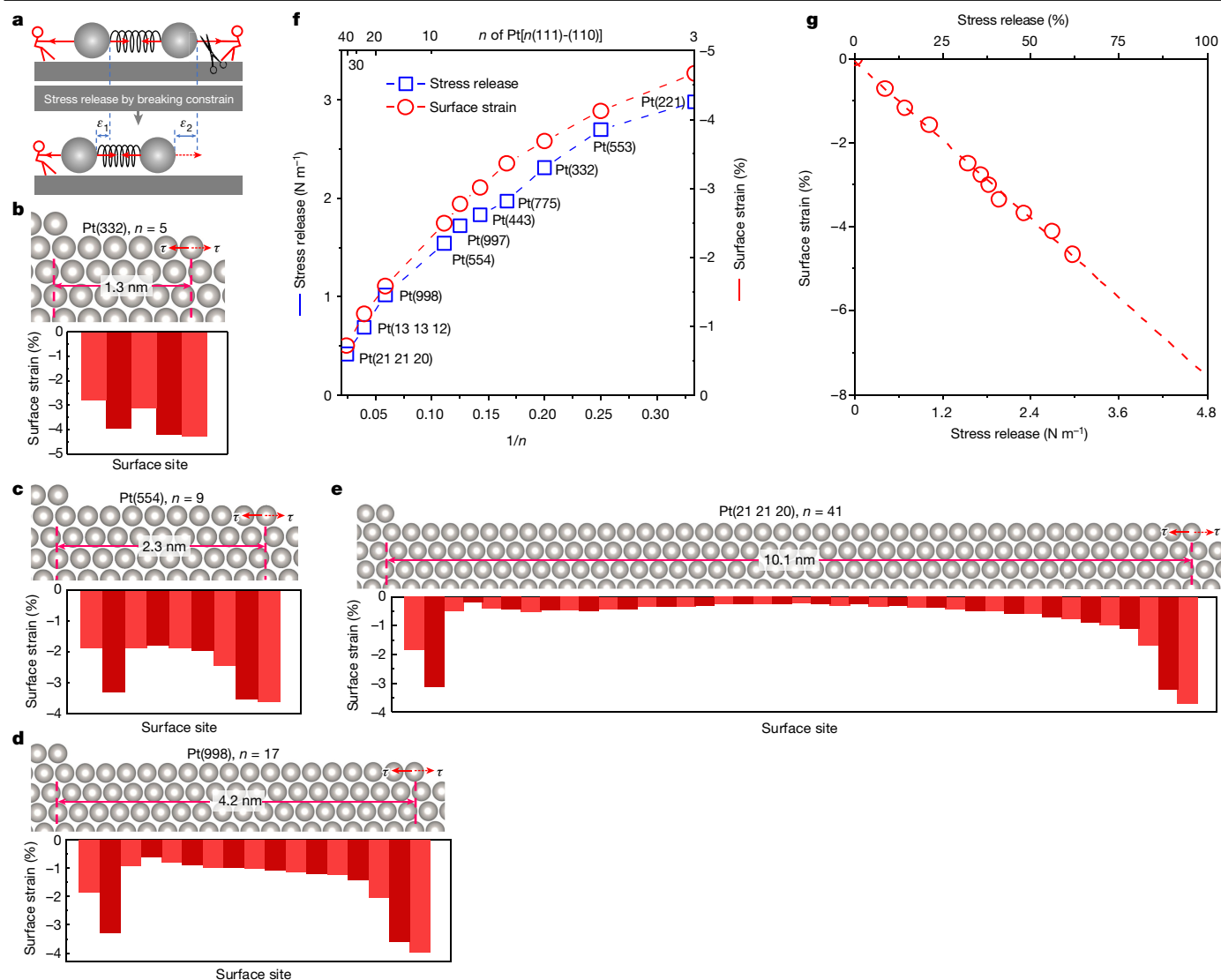
Fig. 1 | The relationship between surface stress release and surface strain generation of stepped Pt(111) surfaces. These stepped Pt(111) surfaces with (110) type step facets can be expressed as $n(111)–(110)$. n is the number of atomic rows on the (111) terrace, which is from 3 to 41 in the current work. **a**, Intrinsic tensile surface stress (τ), and the mechanism of spontaneous surface stress release by breaking symmetry constrain and simultaneous generation of compressive surface strain (ε). **b**–**e**, Side view (upper panels) and atomic site-resolved surface strain (lower panels) of Pt(332) (**b**), Pt(554) (**c**), Pt(998) (**d**) and Pt(21 21 20) (**e**) surfaces with terrace width from 1.3 nm ($n = 5$) to 10.1 nm ($n = 41$), as indicated by double arrow lines. Surface sites correspond to atoms in the top layer of the side views. **f**, The correlation of stress release and average strain with respect to the atomic row n. **g**, The relationship between stress release and average surface strain.

−3.7% and −0.3% on the Pt atoms at the step edge and in the middle of the terrace, respectively (Fig. 1e). These values are also dependent on the terrace width, with the maximum strain increasing to −5.5% and the minimum strain increasing to −3.8% on the Pt(221) surface (Fig. 1b–e and Extended Data Fig. 2).

It has been well established that surface strain modifies the electronic structures and reactivity of surface atoms[14–20]. The aforementioned atomic site-specific strain (Fig. 1b–e) suggests that electronic structures and reactivity of the stepped surfaces are also atomic site specific. To probe these effects, we calculate the d-band centre, a descriptor of surface electronic structures that correlates with catalytic properties, and the OH adsorption energy, a well-known descriptor of the ORR activity. Indeed, both the d-band centre and the OH adsorption energy are sensitive to the geometric location of the atomic site and the terrace width, as is the case for surface strain (Fig. 2 and Extended Data Fig. 3). For the d-band centres, there is generally a down-shift for all terrace atoms that is proportional to the local strain compared to

that of Pt(111). For example, for Pt(21 21 20), the down-shift is ~0.1 eV for Pt atoms around the step edge, where the strain is large, but only 0.01 eV for atoms in the middle of the terrace, where the strain is much smaller. The shifts in the d-band centre depend on the terrace width, with the maximum and minimum values of the down-shifting increasing to 0.14 eV and 0.08 eV, respectively, for Pt(332) with a terrace width of 1.3 nm (Fig. 2a).

As a down-shift of the d-band centre generally indicates increasing inertness of surface atoms, the correlation between d-band centres and site-specific strain suggests that surface atomic sites with larger compressive strain interact less strongly with adsorbates. This is indeed observed for OH adsorption, which is weakened on all terrace sites of stepped surfaces in comparison to Pt(111), with the weakening being proportional to the local strain and the corresponding d-band centre (Fig. 2 and Extended Data Fig. 3). For example, the maximum reduction in binding strength, which is in the range of 0.06–0.11 eV, is on terrace sites near the step edges where large site-specific strain and large
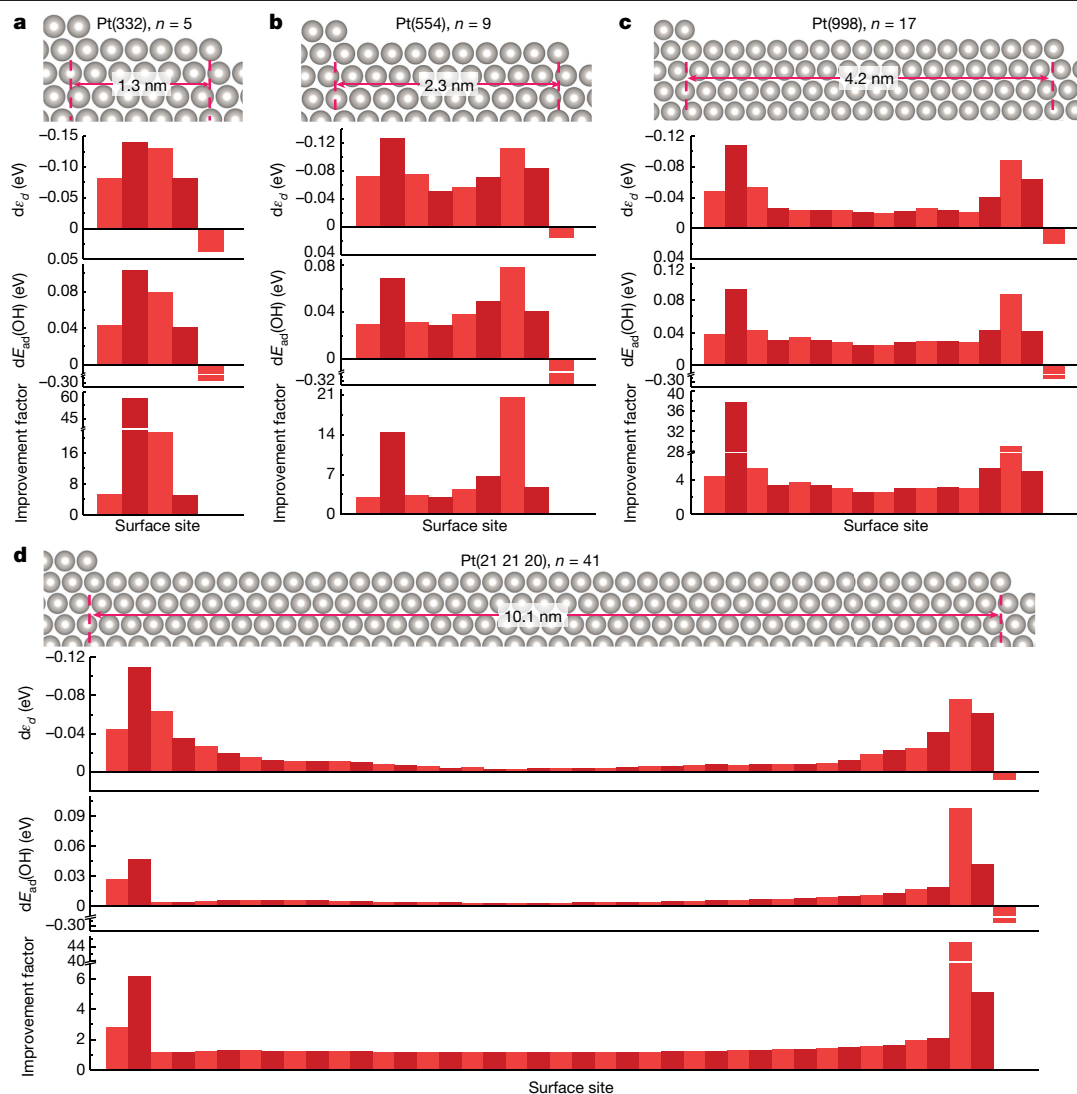
Fig. 2 | Atomic site-resolved electronic structure, surface reactivity and ORR activity of stepped Pt(111) surfaces. a–d, Side view (upper panels) and atomic site-resolved d-band centre shift ($d\varepsilon_d$), OH adsorption energy shift (dE_{ad}(OH)) and predicted ORR improvement factors of Pt(332) (**a**), Pt(554) (**b**), Pt(998) (**c**) and Pt(21 21 20) (**d**) with respect to that of the Pt(111) surface. Surface sites correspond to atoms in the top layer of the side views.

downshifts of the d-band centre are found. It is worth noting that the above results can also explain the site-specific hydrogen adsorption on Pt monolayer island-modified Ru(0001) surfaces[21].

The large inhomogeneities in surface electronic structures and adsorbate binding energies on terrace atoms with identical local coordination provide a compact explanation for the large errors in the quantitative prediction of catalytic activity based on the classic categorization of discrete active sites[7,8,11,12]. The results additionally suggest that the catalytic activity of stepped surfaces is significantly more complex than that implied by the assumption that reactivity is identical for all terrace atoms. Specifically, as perfect Pt(111) single-crystal surfaces are well known to bind too strongly to reaction intermediates for common electrocatalytic reactions (such as the ORR[22]) compared with optimal catalysts on volcano plots, large compressive strain and notable weakening of OH adsorption near the step edges leads to clusters of highly active atomic sites, as catalytic activity depends on the binding energy of reaction intermediates exponentially (see Methods for more details). Among them, the atoms on the upper and lower terraces that are two rows away from the step edges are the most active sites for ORR, with an enhancement factor of approximately 50 times compared to that of perfect Pt(111). The activity then decreases modestly for atomic sites

that are further from the step edges. The resulting spatial distribution of atomic site-specific ORR activities has two maxima, with one maximum on each side of the step edge (Fig. 2), resembling a two-towered suspension bridge. This result provides an atomic-level, site-resolved interpretation of the high-activity zone around step-type defects that was previously observed through electrochemical scanning tunnelling microscopy[1], and related hypotheses for the modified adsorption and catalysis near the step edges[9,23].

As a consequence of this highly inhomogeneous activity distribution, a small fraction of the terrace atoms, near the step edges, dominate the total activity. For example, for Pt(21 21 20), four rows of platinum atoms near step edges, corresponding to less than 10% of the terrace area, contribute over 50% of the overall ORR activity. This enhancement is, however, counterbalanced by the remaining >90% of the terrace, which exhibits much smaller activity enhancements compared to Pt(111), leading to only modest enhancements when averaged over the entire surface. In turn, the presence of high-activity sites near steps, and low-activity sites in the middle of terraces, suggests that reducing the terrace width is a plausible strategy to enhance the overall ORR activity. This is because narrow terraces not only increase the fraction of the high-activity sites, but also increase the minimum enhancement
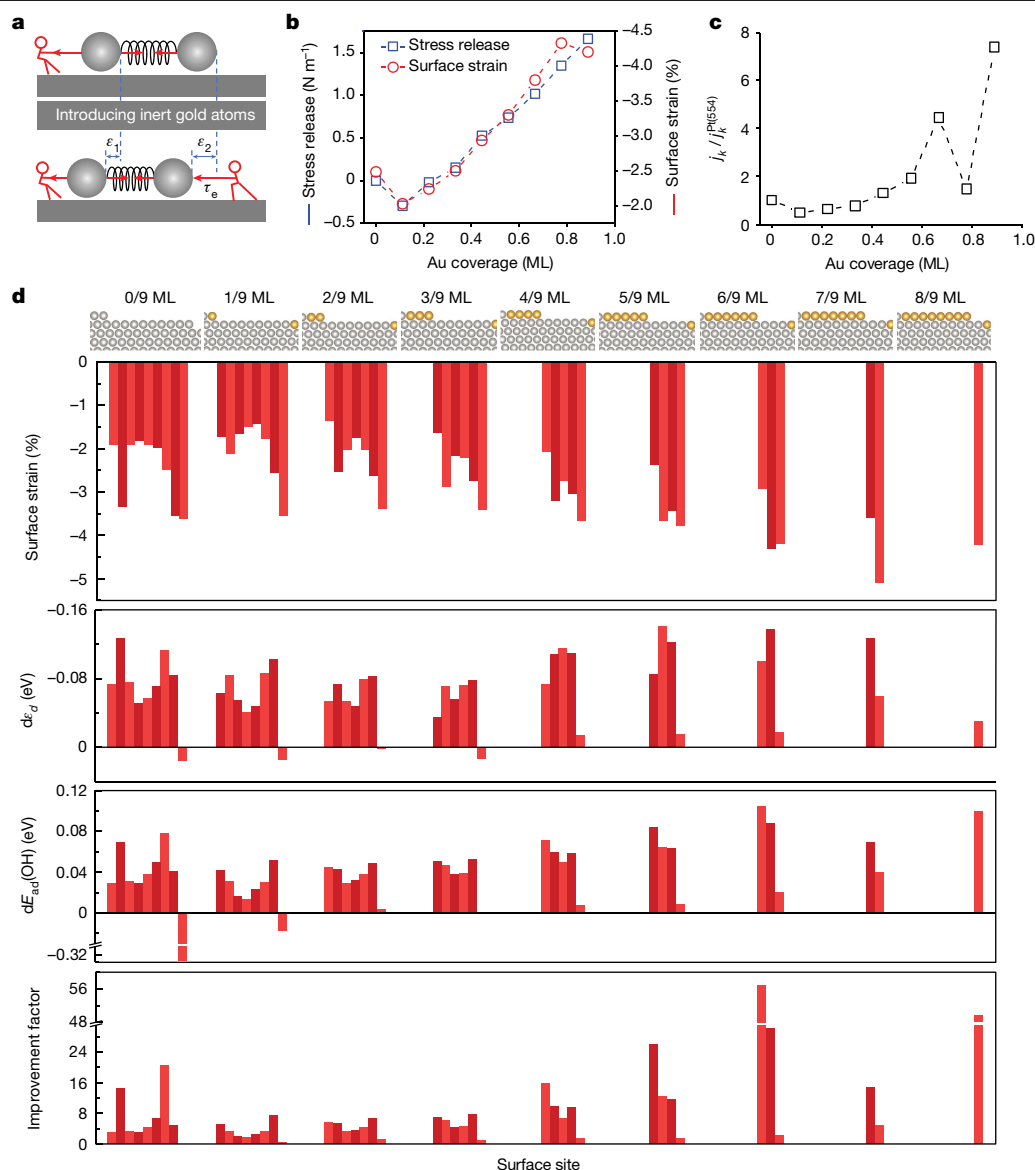
Fig. 3 | The response of residual surface stress, surface strain, surface electronic structure, surface reactivity and ORR activity with respect to external forces. a, Mechanism of generating extra compressive strain by releasing residual tensile surface stress through external compressive stress (τ_e). **b**, Stress release and surface strain of Pt(554) with 0 ML to 8/9 ML of Au at the step edge. **c**, Predicted enhancement of ORR activity of Pt(554) with respect to the coverage of Au. To reduce the errors induced by reference states and at the same time highlight the impact of Au deposition, the predicted ORR enhancement in **c** is normalized to that of Pt(554). **d**, Side view (upper panels) and atomic site-resolved surface strain, d-band centre shift ($d\varepsilon_d$), OH adsorption energy shift ($dE_{ad}(OH)$) and ORR improvement factor of Au/Pt(554) with respect to that of Pt(111), with the coverage of Au from 0 ML to 8/9 ML. Surface sites correspond to atoms in the top layer of the side views.

of the low-activity sites. For example, on Pt(998), with a terrace width of 4.2 nm, the entire terrace maintains an enhancement factor of over 150% (Fig. 2c) compared to perfect Pt(111), whereas for Pt(554) and Pt(332), with terrace widths of 2.3 nm and 1.3 nm, the minimum enhancement factors on the terraces increase to 300% and 500%, respectively (Fig. 2a,b). As a consequence, the average activity increases with decreasing terrace width until the terraces become so small that the step edges with lower activity begin to affect the overall activity (Extended Data Fig. 5). Such a trend is in excellent agreement with the terrace width-dependent ORR activities reported in the literature[9,24,25], except for that preceded by the hydrogen peroxide reduction reaction[26]. We suspect this latter may have undergone surface reconstruction, as indicated by the similar activity to that of much wider terraces[25]. We find that the above correlation between terrace width-dependent stress release, atomic site-specific strain and ORR activity is applicable to stepped Pt(111) surfaces with (100)-type steps, although the magnitude is smaller in comparison to surfaces with (110)-type steps (Extended Data Figs. 6, 7 and 8). Such a dependence on the symmetry of the steps is consistent with that observed in a previous experiment[9], which further confirms the crucial role played by stress release and atomic site-specific strain in the enhancement of ORR activity.

To demonstrate the flexibility and generality of using surface stress release, inhomogeneous strain fields and atomic site-specific reactivity enhancement to tune catalytic properties, we further discuss how such an effect can be achieved via external stress, by the selective deposition of heteroatoms at Pt step edges. Here, we chose heteroatomic Au as an example. Au has a larger lattice constant than Pt, and so depositing Au at the step edge exerts compressive surface stress on terrace Pt atoms, which can serve as the driving force for the release of residual tensile stress (Fig. 3a). In addition, Au is relatively inert for the ORR in
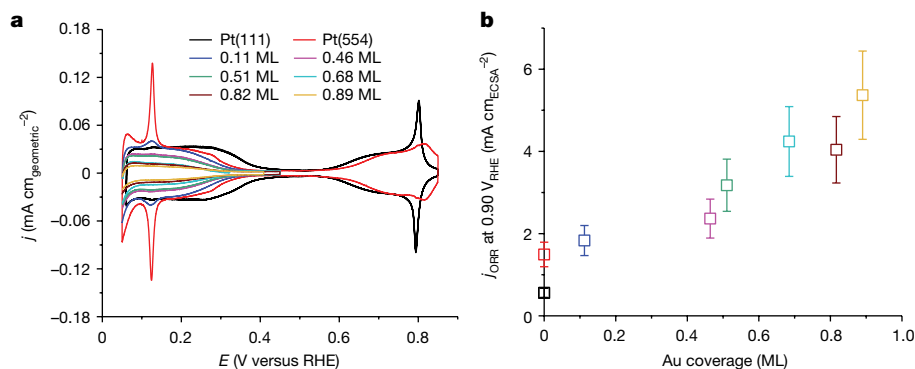
Fig. 4 | ORR activity of Pt(554) surfaces in response to the coverage of Au deposited at the step edge. a,b, CV (**a**) and ORR (**b**) current at 0.9 V_{RHE} for Pt(554) with 0 ML to 0.9 ML Au. CV and ORR currents are normalized to geometric surface area and electrochemical surface area (ECSA), respectively. Electrochemical surface areas were calculated on the basis of the CVs from 0.05–0.45 V_{RHE}. Error bars represent ±2× standard deviation to cover ~95% of the spread.

acidic solutions[27–29], and thus its effect on Pt surface stress and catalytic activity can be investigated without any direct contribution of the Au itself to the ORR activity.

Deposition of Au occurs preferentially along the step edge, as demonstrated by the favourable formation energy of −0.3 eV per Au. The magnitude of the induced surface stress and strain fields depends on the number of rows of Au that are deposited parallel to the edge. For example, on a Pt(554) surface with a terrace width of 9 atoms, a single row of Au atoms has little impact on the strain (Fig. 3b). However, the stress release and compressive surface strain of exposed Pt atoms increase as additional rows of Au atoms are deposited. Although the exact distribution of strain is complex, there is generally an increase in strain with increasing Au coverage, leading to a maximum average compressive strain of −4.3% at a coverage of 7/9 monolayers (ML) of Au (Fig. 3b). There are similarly complex profiles for the electronic structure and adsorption energies, but the general trends are consistent, with larger compressive strain induced by larger releases of residual stress leading to larger downshifts of the *d*-band centre and weaker OH binding energies (Fig. 3d). Analogous trends are seen for the ORR activity of exposed surface Pt atoms, which is relatively constant at low Au coverage and gradually increases with increasing Au coverage (Fig. 3c). A notable activity increase is observed when the Au coverage increases to 4/9 ML and higher, due to increasing strain in exposed Pt sites and the disappearance of terrace sites with small strain. The latter is similar to the effect of decreasing the terrace width of the stepped surface, that is, there is more substantial activity enhancement at a terrace width of $n \le 8$ (Extended Data Fig. 5). The ORR activity decreases at 7/9 ML, probably because the strain effects are convoluted with the electronic effects, and then increases again before the terrace is fully covered by Au.

To verify the predicted ORR activity trends induced by Au adsorption, we performed electrochemical experiments on Pt(554) with Au atoms at the step edge (Fig. 4 and Extended Data Figs. 9 and 10). Au atoms with coverages ranging from 0.1 ML to 0.9 ML were introduced through Au electrodeposition, and evaluated on the basis of cyclic voltammetry. The preferential deposition at the step edge is evidenced by the disappearance of the (110) step edge feature at approximately 0.12 V_{RHE} (RHE, reversible hydrogen electrode, Fig. 4a)[30–32], which is fully consistent with the computational predictions. ORR polarization curves indicate that the variation of specific activities at coverages <0.5 ML is within measurement error, and there is no substantial increase until the coverage is higher than 0.5 ML (Fig. 4b). The specific activity decreases slightly at 0.8 ML Au before increasing again (Fig. 4b). These activity trends are in remarkable agreement with our computational predictions (Fig. 3c). The results confirm the precision and flexibility that can be achieved in controlling surface reactivity by manipulating surface stress.

In this work, we have demonstrated that surface stress release, caused by surface defects or heteroatom deposition, can lead to highly inhomogeneous surface strain fields. These inhomogeneities lead to highly localized changes in surface electronic structure and adsorption energies, which modify site-specific activity by orders of magnitude, and consequently impact the overall activity. These phenomena succinctly explain the trends in ORR activity on stepped Pt(111) surfaces, which have been intensively debated in the literature, and which increase with decreasing terrace width[8,9,24,33], leading to high ORR activity of jagged Pt nanowires with rich terraces of 3–4 atoms wide[34]. In addition to ORR, general trends in catalytic activity in response to surface strain have been observed for many other chemical reactions[20,35,36]. Thus, manipulation of surface stress and strain fields is a flexible and effective strategy to tune the catalytic activity of chemical reactions that are sensitive to surface strain.

Online content

Any methods, additional references, Nature Portfolio reporting summaries, source data, extended data, supplementary information, acknowledgements, peer review information; details of author contributions and competing interests; and statements of data and code availability are available at https://doi.org/10.1038/s41586-024-07090-z.

1. Pfisterer, J. H., Liang, Y., Schneider, O. & Bandarenka, A. S. Direct instrumental identification of catalytically active surface sites. *Nature* **549**, 74–77 (2017).
2. Cao, L. et al. Identification of single-atom active sites in carbon-based cobalt catalysts during electrocatalytic hydrogen evolution. *Nat. Catal.* **2**, 134–141 (2019).
3. Jia, Y. et al. Identification of active sites for acidic oxygen reduction on carbon catalysts with and without nitrogen doping. *Nat. Catal.* **2**, 688–695 (2019).
4. Zambelli, T., Wintterlin, J., Trost, J. & Ertl, G. Identification of the "active sites" of a surface-catalyzed reaction. *Science* **273**, 1688–1690 (1996).
5. Liang, Y., McLaughlin, D., Csoklich, C., Schneider, O. & Bandarenka, A. S. The nature of active centers catalyzing oxygen electro-reduction at platinum surfaces in alkaline media. *Energy Environ. Sci.* **12**, 351–357 (2019).
6. Kajiwara, R., Asaumi, Y., Nakamura, M. & Hoshi, N. Active sites for the hydrogen oxidation and the hydrogen evolution reactions on the high index planes of Pt. *J. Electroanal. Chem.* **657**, 61–65 (2011).
7. Calle-Vallejo, F. et al. Finding optimal surface sites on heterogeneous catalysts by counting nearest neighbors. *Science* **350**, 185–189 (2015).
8. Calle-Vallejo, F. et al. Why conclusions from platinum model surfaces do not necessarily lead to enhanced nanoparticle catalysts for the oxygen reduction reaction. *Chem. Sci.* **8**, 2283–2289 (2017).
9. Hoshi, N., Nakamura, M. & Hitotsuyanagi, A. Active sites for the oxygen reduction reaction on the high index planes of Pt. *Electrochim. Acta* **112**, 899–904 (2013).
10. Neugebohren, J. et al. Velocity-resolved kinetics of site-specific carbon monoxide oxidation on platinum surfaces. *Nature* **558**, 280–283 (2018).
11. Wang, H. & An, W. Promoting the oxygen reduction reaction with gold at step/edge sites of Ni@ AuPt core–shell nanoparticles. *Catal. Sci. Technol.* **7**, 596–606 (2017).
12. Rück, M., Bandarenka, A., Calle-Vallejo, F. & Gagliardi, A. Oxygen reduction reaction: rapid prediction of mass activity of nanostructured platinum electrocatalysts. *J. Phys. Chem. Lett.* **9**, 4463–4468 (2018).

Article

13. Ha, Y. et al. In situ surface stress measurement and computational analysis examining the oxygen reduction reaction on Pt and Pd. *Electrochim. Acta* **260**, 400–406 (2018).
14. Wang, L. et al. Tunable intrinsic strain in two-dimensional transition metal electrocatalysts. *Science* **363**, 870–874 (2019).
15. Mavrikakis, M., Hammer, B. & Nørskov, J. K. Effect of strain on the reactivity of metal surfaces. *Phys. Rev. Lett.* **81**, 2819–2822 (1998).
16. Strasser, P. et al. Lattice-strain control of the activity in dealloyed core–shell fuel cell catalysts. *Nat. Chem.* **2**, 454–460 (2010).
17. Wang, H. et al. Direct and continuous strain control of catalysts with tunable battery electrode materials. *Science* **354**, 1031–1036 (2016).
18. Khorshidi, A., Violet, J., Hashemi, J. & Peterson, A. A. How strain can break the scaling relations of catalysis. *Nat. Catal.* **1**, 263–268 (2018).
19. Streibel, V., Choksi, T. S. & Abild-Pedersen, F. Predicting metal–metal interactions. I. The influence of strain on nanoparticle and metal adlayer stabilities. *J. Chem. Phys.* **152**, 094701 (2020).
20. He, T. et al. Mastering the surface strain of platinum catalysts for efficient electrocatalysis. *Nature* **598**, 76–81 (2021).
21. Sakong, S., Fischer, J. M., Mahlberg, D., Behm, R. J. & Groß, A. Influence of step and island edges on local adsorption properties: hydrogen adsorption on Pt monolayer island modified Ru(0001) electrodes. *Electrocatalysis* **8**, 530–539 (2017).
22. Seh, Z. W. et al. Combining theory and experiment in electrocatalysis: insights into materials design. *Science* **355**, eaad4998 (2017).
23. Hartmann, H., Diemant, T., Bansmann, J. & Behm, R. J. Interaction of CO and deuterium with bimetallic, monolayer Pt-island/film covered Ru(0001) surfaces. *Phys. Chem. Chem. Phys.* **14**, 10919–10934 (2012).
24. Kuzume, A., Herrero, E. & Feliu, J. M. Oxygen reduction on stepped platinum surfaces in acidic media. *J. Electroanal. Chem.* **599**, 333–343 (2007).
25. Gómez-Marín, A. M. & Feliu, J. M. Oxygen reduction on nanostructured platinum surfaces in acidic media: promoting effect of surface steps and ideal response of Pt(111). *Catal. Today* **244**, 172–176 (2015).
26. Briega-Martos, V., Herrero, E. & Feliu, J. M. Hydrogen peroxide and oxygen reduction studies on Pt stepped surfaces: surface charge effects and mechanistic consequences. *Electrochim. Acta* **334**, 135452 (2020).
27. Wang, C. et al. Multimetallic Au/FePt$_3$ nanoparticles as highly durable electrocatalyst. *Nano Lett.* **11**, 919–926 (2011).
28. Bergbreiter, A., Alves, O. B. & Hoster, H. E. Entropy effects in atom distribution and electrochemical properties of Au$_x$Pt$_{1-x}$/Pt(111) surface alloys. *ChemPhysChem* **11**, 1505–1512 (2010).
29. Brimaud, S., Engstfeld, A., Alves, O. & Behm, R. Structure–reactivity correlation in the oxygen reduction reaction: activity of structurally well defined Au$_x$Pt$_{1-x}$/Pt (111) monolayer surface alloys. *J. Electroanal. Chem.* **716**, 71–79 (2014).
30. Kodama, K., Jinnouchi, R., Takahashi, N., Murata, H. & Morimoto, Y. Activities and stabilities of Au-modified stepped-Pt single-crystal electrodes as model cathode catalysts in polymer electrolyte fuel cells. *J. Am. Chem. Soc.* **138**, 4194–4200 (2016).
31. McCrum, I. T. & Koper, M. T. The role of adsorbed hydroxide in hydrogen evolution reaction kinetics on modified platinum. *Nat. Energy* **5**, 891–899 (2020).
32. Sheng, W. et al. Correlating hydrogen oxidation and evolution activity on platinum at different pH with measured hydrogen binding energy. *Nat. Commun.* **6**, 5848 (2015).
33. Bandarenka, A. S., Hansen, H. A., Rossmeisl, J. & Stephens, I. E. Elucidating the activity of stepped Pt single crystals for oxygen reduction. *Phys. Chem. Chem. Phys.* **16**, 13625–13629 (2014).
34. Li, M. et al. Ultrafine jagged platinum nanowires enable ultrahigh mass activity for the oxygen reduction reaction. *Science* **354**, 1414–1419 (2016).
35. Jiao, L., Liu, E., Hwang, S., Mukerjee, S. & Jia, Q. Compressive strain reduces the hydrogen evolution and oxidation reaction activity of platinum in alkaline solution. *ACS Catal.* **11**, 8165–8173 (2021).
36. Rossmeisl, J. et al. Bifunctional anode catalysts for direct methanol fuel cells. *Energy Environ. Sci.* **5**, 8335–8342 (2012).

Methods

Computational method details

Density functional theory calculation parameters. Periodic density functional theory (DFT) calculations are performed with the Vienna Ab-initio Simulation Package (VASP)[37,38], using the projector-augmented wave method[39]. Exchange-correlation energies are evaluated using the generalized gradient approximation with the Perdew–Burke–Ernzerhof functional[40]. A cutoff energy of 400 eV is used for the plane wave basis. The geometries are optimized until the maximum atomic forces are smaller than 0.01 eV $Å^{-1}$, and the convergence criteria for the total energies are set as 10^{-5} eV. The calculated lattice constant of face-centred cubic Pt is 3.977 Å through minimizing the stress tensor.

For surface stress and surface strain calculations, Pt(111) and stepped Pt(111) surfaces with notation of n(111)–(110) and n(111)–(100), which consist of (111) terraces with a terrace width of n atomic rows separated by monoatomic (110) and (100) step facets, respectively, are modelled by slabs with a thickness of 7 ML in [111]. The slabs and their images are separated by 14 Å of vacuum along the z direction. The k-point meshes (k_1, k_2, k_3) are selected for those surfaces so that their product with the norms of the lattice vectors (a_1, a_2, a_3) in Å is (a_1k_1, a_2k_2, a_3k_3) > (30 Å, 30 Å, 30 Å). All atoms are allowed to relax in the calculation of surface stress. For OH adsorption calculations, stepped Pt surfaces with a terrace width <17 atoms are also modelled by slabs with a thickness of 7 ML in [111]. The topmost three layers and the adsorbates are allowed to relax, whereas the remaining layers are fixed in their optimized configuration from surface stress calculations. However, for Pt(998) and Pt(21 21 20) with a terrace width of 17 and 41 atom rows, respectively, surfaces are modelled by 4 ML slabs, with the bottom two layers fixed in their optimized configuration. The (2 × 1) and (1 × 2) supercells are used for n(111)–(110) and n(111)–(100) surfaces, respectively. For accurate calculations of relative adsorption energy, Pt(111) surfaces are modelled by c(4 × n) and c(4 × (n + 1)) supercells with the same thickness as that of n(111)–(110) surfaces, when n is an even and odd number, respectively. The reaction intermediates are adsorbed onto the top side of the slab. An orthorhombic box (14 × 15 × 16 $Å^3$) and a single k-point (0.25, 0.25, 0.25) for the Brillouin zone sampling are used for the calculation of gas-phase H_2O and H_2. For OH and OOH adsorption on Pt surfaces, top sites are considered, as they are the most favourable sites at water/Pt interfaces. The OH energies on all surface sites are calculated on stepped Pt surfaces.

Au deposition. For Au atoms deposited at the step edge of the Pt(554) surface, the formation energy (E_f) of the Au atom row is calculated using,

$$E_f = \frac{E_{tot}[NAu/Pt(554)] - E_{tot}[Pt(554)] - NE_{tot}[Au]}{N} \quad (1)$$

$E_{tot}[Au]$, $E_{tot}[Pt(554)]$ and $E_{tot}[NAu/Pt(554)]$ are the total energies of Au bulk, Pt(554)-(1 × 1) and Pt(554)-(1 × 1) with N rows of Au atoms deposited at the step edge, respectively.

Surface stress and surface strain. Surface stress (σ_{xx} and σ_{yy}) is calculated using the stress theorem developed by Nielsen and Martin[41], which is obtained by

$$\sigma_{ij} = \frac{c}{2}\tau_{ij} \quad (2)$$

where c is the supercell height in the z direction and τ_{ij} is the diagonal component of the stress tensor, for which τ_{xx} and τ_{yy} are the x and y direction of the supercell, respectively.

We find the surface stress in the direction along the steps (σ_{xx} of n(111)–(110) and σ_{yy} of n(111)–(100)) is similar to that of (111), but surface stresses in the direction perpendicular to the steps (σ_{yy} of n(111)–(110) and σ_{xx} of n(111)–(100)) are smaller than that of (111) due to surface

stress release (Extended Data Fig. 1 and Extended Data Table 1). Stress release is calculated as $\Delta\sigma$:

$$\Delta\sigma = \sigma_{Pt(111)} - \sigma_{Pt(kkl)/Pt(kll)} \quad (3)$$

where $\sigma_{Pt(111)}$ and $\sigma_{Pt(kkl)/Pt(kll)}$ are surface stress of Pt(111) and surface stresses of Pt(kkl) (or Pt(kll)) in the direction perpendicular to the steps, respectively. For the Pt(554) surface with Au deposition, stress release is calculated as follows

$$\Delta\sigma_{yy} = \sigma_{yy-Pt(554)} - \sigma_{yy-Au/Pt(554)} \quad (4)$$

where $\sigma_{yy-Au/Pt(554)}$ and $\sigma_{yy-Pt(554)}$ are the surface stresses σ_{yy} of Pt(554) with and without Au deposition.

Surface stress release of stepped Pt(111) surfaces is accompanied by contraction of the surface atoms, that is, the generation of compressive strain. In our DFT calculations, average surface strain is calculated using:

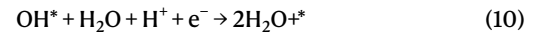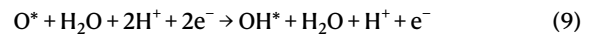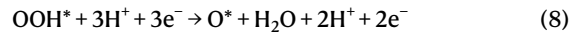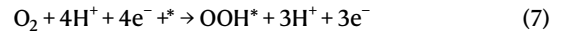$$\varepsilon = \frac{l - l_0}{l_0} \times 100\%, \quad (5)$$

where l_0 and l are the terrace width of a stepped (111) surface with an n atomic row terrace before and after surface relaxation, respectively.
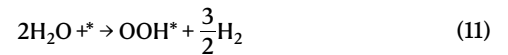
The atomic site-specific strain is calculated as:

$$\varepsilon = \frac{d - d_0}{d_0} \times 100\%, \quad (6)$$

where d_0 and d are the distance of an atom from the nearest-neighbour atoms of the adjacent row before and after surface relaxation, respectively.

Surface ORR reactivity. For ORR, a well-established association mechanism proceeds through four steps, as below:

$$O_2 + 4H^+ + 4e^- + {}^* \rightarrow OOH^* + 3H^+ + 3e^- \quad (7)$$

$$OOH^* + 3H^+ + 3e^- \rightarrow O^* + H_2O + 2H^+ + 2e^- \quad (8)$$

$$O^* + H_2O + 2H^+ + 2e^- \rightarrow OH^* + H_2O + H^+ + e^- \quad (9)$$

$$OH^* + H_2O + H^+ + e^- \rightarrow 2H_2O + {}^* \quad (10)$$

where the asterisk (*) denotes a free adsorption site on the surface. The adsorption energies of reaction intermediates (OOH*, O* and OH*) are calculated with H_2O and H_2 as references:

$$2H_2O + {}^* \rightarrow OOH^* + \frac{3}{2}H_2 \quad (11)$$

$$H_2O + {}^* \rightarrow O^* + H_2 \quad (12)$$

$$H_2O + {}^* \rightarrow OH^* + \frac{1}{2}H_2 \quad (13)$$

The free energies of adsorption are obtained by correcting the DFT energies for zero point energy (ZPE), integrated heat capacities (δH), entropy (S) and solvation energy (E_{sol}) via

$$G = E_{DFT} + ZPE + \delta H - TS + E_{sol} \quad (14)$$

For gas-phase species (H_2O and H_2), ZPE, δH and S are obtained from standard thermodynamic tables[42]. For adsorption of reaction

intermediates (O*, OH* and OOH*), the corresponding data are estimated from the vibrational frequencies within the harmonic oscillation. Solvation energies of OH* and OOH* are calculated on the basis of the adsorption energy difference between an OH/OOH and the OH/OOH in the H_2O layer[43,44]. For O* and OH*, the free energies are further corrected to match experimental values on Pt(111). The correction of OOH* is estimated on the basis of the formation energy of H_2O_2 and H_2O (ref. 44). All corrections are listed in Extended Data Table 2.

The free energies of reactions (7)–(10) are calculated as follows:

$$\Delta G_1 = \Delta G_{ad}(OOH) - 4.92 \tag{15}$$

$$\Delta G_2 = \Delta G_{ad}(O) - \Delta G_{ad}(OOH) \tag{16}$$

$$\Delta G_3 = \Delta G_{ad}(OH) - \Delta G_{ad}(O) \tag{17}$$

$$\Delta G_4 = -\Delta G_{ad}(OH) \tag{18}$$

where ΔG_i is the reaction free energy at $U = 0$ V. The reaction free energies at potential U are written as:

$$\Delta G_1(U) = \Delta G_1 + eU = \Delta G_{ad}(OOH) - 4.92 + eU \tag{19}$$

$$\Delta G_2(U) = \Delta G_2 + eU = \Delta G_{ad}(O) - \Delta G_{ad}(OOH) + eU \tag{20}$$

$$\Delta G_3(U) = \Delta G_3 + eU = \Delta G_{ad}(OH) - \Delta G_{ad}(O) + eU \tag{21}$$

$$\Delta G_4(U) = \Delta G_4 + eU = -\Delta G_{ad}(OH) + eU \tag{22}$$

If we define $U = \min(U_1, U_2, U_3, U_4)$ as the maximum potential at which the forward reaction has no thermodynamic barrier ($\Delta G_i(U_i) = 0$), then the minimum overpotential is 1.23 U. This, 1.23 V is the maximum cell voltage. For the Pt(111) surface, the potential-determining step is OH* protonation to produce H_2O, in which U_4 ($\Delta G_4(U_4) = 0$) is the maximum potential[14,43–49].

The rate constant of the Pt(111) surface at maximum potential $U^{(111)}$ can be written as

$$k^{Pt(111)}(U^{(111)}) = k_0 e^{-\Delta G(U^{(111)})/k_bT} \tag{23}$$

The prefactor, k_0, includes all of the details of the proton transfer to the surface and recombination with the electron. For stepped surfaces, the rate constant of the stepped Pt(hkl) surface on the atomic site i is

$$k_i^{Pt(hkl)}(U_i^{(hkl)}) = k_0 e^{-\Delta G(U_i^{(hkl)})/k_bT} \tag{24}$$

In this work, we focus on atomic site-specific ORR activity versus that on the Pt(111) surface. The improvement factor (N) of the atomic site i on stepped surfaces is obtained by calculating

$$N = \frac{k_i^{Pt(hkl)}(U_i^{(hkl)})}{k^{Pt(111)}(U^{(111)})} = e^{(U_i^{(hkl)} - U^{(111)})/k_bT} \tag{25}$$

In units of current density, the rate constant of Pt(111) is

$$j_k^{Pt(111)}(U^{(111)}) = \frac{4e}{A} k_0 e^{-\Delta G(U^{(111)})/k_bT} \tag{26}$$

where A is the surface area per site. For the stepped surface, the current density is weighted based on the calculated rate on all atomic sites.

$$j_k^{Pt(hkl)}(U^{(hkl)}) = \frac{4e}{nA} k_0 \sum_{i=1}^{n} e^{-\Delta G(U_i^{(hkl)})/k_bT} \tag{27}$$

The relative current density of the stepped surface versus that on Pt(111) is,

$$\frac{j_k^{Pt(hkl)}}{j_k^{Pt(111)}} = \frac{1}{n} \sum_{i=1}^{n} e^{-\Delta G(U_i^{(hkl)} - U^{(111)})/k_bT} \tag{28}$$

Details of experimental method

Cleaning and preparation of electrochemical cells. Glassware and PTFE parts used in the electrochemical cell setup and electrolyte preparation were first soaked in a 0.5 M H_2SO_4 solution (Sigma-Aldrich, 95.0–97.0%) containing 1 g L^{-1} KMnO₄ (Sigma-Aldrich, ≥99.0%) for at least 48 h at 298 K to oxidize organic compounds. The glassware was then removed from the H_2SO_4/KMnO₄ solution, rinsed three times with ultrahigh purity (UHP) water (Merck Milli-Q IQ 7000, <5 ppb total organic content, 18.2 MΩ cm at 298 K), then submerged in piranha solution (approximately 1 M H_2SO_4 (Sigma-Aldrich, 95.0–97.0%) and approximately 6% H_2O_2 (Merck, 35%)) at 298 K to dissolve traces of KMnO₄, MnO₂ and other oxidized products for at least 30 min. The glassware was then rinsed three times with UHP water and an additional 5–10 times with boiling UHP water at 373 K.

Electrochemical cell and electrode preparation. The disk-type and bead-type Pt single crystals (purchased from MaTeck and Surface Preparation Laboratory) were flame annealed at the tip of the blue flame from two butane torches (Toolcraft MT-770S with flame classics universal gas lighter refill) for at least 3 min. The disk was then quickly transferred (<2 s) to a cooling cell purged with 1:4 v/v H_2:Ar at approximately 500 sccm bubbled through UHP H_2O to cool[50,51]. After cooling to room temperature (approximately 3–10 min), the Pt(111) was protected by a droplet of UHP H_2O from the cooling cell before removal and transfer (<10 s) in ambient air to the electrochemical cell, with efforts to minimize the transfer time.

Two electrochemical cells were prepared for all Au deposition and ORR experiments: one dedicated for Au deposition, and a second dedicated for ORR measurements. A 0.1 M HClO₄ electrolyte was prepared in both cells and saturated with approximately 100–200 sccm Ar (Linde, 5.0 Grade 99.999%) for 30 min through two apertures in the electrochemical cell: one through the electrolyte and another into the chamber above the electrolyte. When saturated, argon bubbling through the electrolyte was shut off to ensure an unperturbed electrolyte surface, as argon continued to purge the chamber above the electrolyte. The working electrode potential was set to 0.1 V_{RHE} and a hanging-meniscus contact between the working electrode and electrolyte was carefully formed to ensure no undesired currents from edge wetting. When the current reached steady state (typically between 10 s to 4 min), several (typically 6 to 10) cyclic voltammograms were collected between 0.06 and 0.85 V_{RHE} with a scan rate of 50 mV s^{-1}. After completion, the potential was set to 0.1 V_{RHE} before breaking the meniscus between the electrode and the electrolyte solution. This validation was performed with both cells to ensure a quality Pt single crystal and clean 0.1 M HClO₄ electrolyte before proceeding with Au deposition and ORR measurements.

Au deposition. For Au deposition, 0.25×10^{-6} M HAuCl₄ was prepared by adding a calculated volume of 10^{-4} M HAuCl₄ (prepared from HAuCl₄ (Sigma-Aldrich, 99.995% trace metals basis) and UHP water) to the Ar-saturated 0.1 M HClO₄ in the electrochemical cell dedicated for Au deposition, then allowed to saturate with Ar for at least 30 min. To deposit Au, a hanging-meniscus contact with the electrode was formed using a freshly annealed single crystal at 0.1 V_{RHE} and cycling in the H_{UPD} region between 0.06 and 0.45 V_{RHE} at 50 mV s^{-1} was performed (typically between 10 and 600 cycles). This procedure enabled us to visually monitor the Au deposition in real time. When the desired Au coverage was achieved, the meniscus was broken during cycling and transferred to the ORR cell for kinetic measurements.

ORR measurements. For hanging-meniscus rotating disk electrode ORR measurements, O_2 (Linde HiQ Oxygen 5.0, zero grade, ≥99.999%) was bubbled at a rate of approximately 100 sccm through the 0.1 M $HClO_4$ solution for at least 40 min before kinetic measurement. The electrode was protected with a droplet (either UHP water saturated with H_2/Ar for Au-free Pt single crystals after the typical annealing procedure, or a droplet with the Ar-saturated $HAuCl_4$/$HClO_4$ electrolyte after Au deposition for Au/Pt single crystals) and installed onto a rotator (Pine Research modulated speed rotator (MSR)). The entire installation process in ambient air took between 5 and 10 min depending on the time required to ensure the axis of the electrode was in line with the rotational axis of the rotator, and that the face of the electrode was horizontal. Once installed onto the MSR, the potential was set to $0.05\,V_{RHE}$, the hanging meniscus was formed and the MSR was set to a predetermined rotation rate (typically 1,600 rpm). Once the current was stable (approximately 5 s), the potential was cycled between 0.05 and $1.0\,V_{RHE}$ at a scan rate of $10\,mV\,s^{-1}$. The ORR limiting current at $0.5\,V_{RHE}$ was used as an indicator for the quality of the rotating meniscus. The limiting current was calculated using the Levich equation[52] (equation (29) and Extended Data Fig. 9), and for an O_2-saturated 0.1 M $HClO_4$ solution, a limiting current of $6.02\,mA\,cm^{-2}$ is predicted (O_2-saturated 0.1 M $HClO_4$ at 23 °C, 1,600 rpm, cycled between 0.05 and $1.0\,V_{RHE}$ at $10\,mV\,s^{-1}$).

$$i/A = 0.2nFD^{\frac{2}{3}}v_0^{-\frac{1}{6}}\omega^{\frac{1}{2}}c_b \tag{29}$$

where i and A are the limiting current and geometric surface area, respectively; n is the number of electrons transferred ($n = 4$ for ORR); F is Faraday's constant ($96485.336521\,C\,mol^{-1}$); D is the diffusion coefficient of reactant ($1.93 \times 10^{-5}\,cm^2\,s^{-1}$); v_0 is the kinetic viscosity of the electrolyte ($1.009 \times 10^{-2}\,cm^2\,s^{-1}$); c_b is the bulk concentration of the reactant in electrolyte ($1.26 \times 10^{-6}\,mol\,cm^{-3}$); and ω is electrode rotation rate in rotations per minute.

However, instead of the geometric surface area, all reported ORR currents are normalized to the ECSA, given by equation (30), which is calculated on the basis of the cyclic voltammograms from 0.05 to $0.45\,V_{RHE}$. Note that for an Au-free electrode, ECSA is equal to the geometric surface area of the single crystal.

$$A_{electrochemical} = \frac{\frac{1}{F}\int_{0.05V_{RHE}}^{0.45V_{RHE}}(i_{Pt} - i_{Au/Pt})dt}{\left(\frac{\rho_{Pt(111)}}{N_A}\right)p} \tag{30}$$

where $A_{electrochemical}$ is the electrochemical surface area; i and t are the current (in amperes) and time (in seconds), respectively; $\rho_{Pt(111)}$ is the density of surface Pt(111) atoms ($1.503 \times 10^{15}\,atoms\,cm^{-2}$); N_A is Avogadro's constant ($6.02214086 \times 10^{23}\,atoms\,mol^{-1}$). Based off the projection and angle of the (111) terraces relative to the single crystal cut, $p = \frac{2n-1}{\sqrt{4 + (2n-1)^2}}$, where n is the length of the (111) terrace length in atoms.

Au removal from single crystal after ORR measurements. Au was removed from Au/Pt electrodes after ORR via etching in concentrated HNO_3 (Merck Millipore, ≥65% Suprapur). The Au/Pt was first submerged for 30 min in HNO_3 then rinsed with UHP water. The electrode was then flame annealed for 15 s, quickly transferred to (<1 s) and quenched in concentrated HNO_3 (Merck Millipore, ≥65% Suprapur), then rinsed with UHP H_2O; this process was repeated a total of about five times. The Au-free Pt single crystal was then confirmed via cyclic voltammetry in Ar-saturated 0.1 M $HClO_4$. This HNO_3 etching process produces a visible mustard-coloured cloud of toxic NO and NO_2 vapours via thermal decomposition of HNO_3 and must be performed where toxic vapours can be safely vented away without exposure to the experimenter (for example, in a fume hood). Recommended

maximum exposure levels documented by the Occupational Safety and Health Administration (OSHA), National Institute for Occupational Safety and Health (NIOSH) and American Conference of Governmental Industrial Hygienists (ACGIH) for NO and NO_2 are of the order of 25 and 5 ppm, respectively.

Data availability

Other data supporting the findings of this study are available in the main text and the extended data. Source data are provided with this paper.

37. Kresse, G. & Furthmüller, J. Efficient iterative schemes for ab initio total-energy calculations using a plane-wave basis set. *Phys. Rev. B* **54**, 11169 (1996).
38. Kresse, G. & Hafner, J. Ab initio molecular dynamics for open-shell transition metals. *Phys. Rev. B* **48**, 13115 (1993).
39. Kresse, G. & Joubert, D. From ultrasoft pseudopotentials to the projector augmented-wave method. *Phys. Rev. B* **59**, 1758 (1999).
40. Perdew, J. P., Burke, K. & Ernzerhof, M. Generalized gradient approximation made simple. *Phys. Rev. Lett.* **77**, 3865 (1996).
41. Nielsen, O. & Martin, R. M. Quantum-mechanical theory of stress and force. *Phys. Rev. B* **32**, 3780 (1985).
42. Chase, M. W. *NIST-JANAF Thermochemical Tables* Vol. 9 (American Chemical Society, 1998).
43. Zeng, Z. & Greeley, J. Characterization of oxygenated species at water/Pt (111) interfaces from DFT energetics and XPS simulations. *Nano Energy* **29**, 369–377 (2016).
44. Wang, L. et al. Plating precious metals on nonprecious metal nanoparticles for sustainable electrocatalysts. *Nano Lett.* **17**, 3391–3395 (2017).
45. Wang, L. et al. Core–shell nanostructured cobalt–platinum electrocatalysts with enhanced durability. *ACS Catal.* **8**, 35–42 (2018).
46. Christensen, R., Hansen, H. A., Dickens, C. F., Nørskov, J. K. & Vegge, T. Functional independent scaling relation for ORR/OER catalysts. *J. Phys. Chem. C* **120**, 24910–24916 (2016).
47. Nørskov, J. K. et al. Origin of the overpotential for oxygen reduction at a fuel-cell cathode. *J. Phys. Chem. B* **108**, 17886–17892 (2004).
48. Greeley, J. et al. Alloys of platinum and early transition metals as oxygen reduction electrocatalysts. *Nat. Chem.* **1**, 552–556 (2009).
49. Martínez, J. I. et al. Universality in oxygen evolution electrocatalysis on oxide surfaces. *ChemCatChem* **3**, 1159–1165 (2011).
50. Hamelin, A. Cyclic voltammetry at gold single-crystal surfaces. Part 1. Behaviour at low-index faces. *J. Electroanal. Chem.* **407**, 1–11 (1996).
51. Kibler, L. A. Preparation and characterization of noble metal single crystal electrode surfaces. *Int. Soc. Electrochem.* **14**, 20 (2003).
52. Bard, A. J. & Faulkner, L. R. Fundamentals and applications: electrochemical methods. *Electrochem. Methods* **2**, 580–632 (2001).
53. Mayrhofer, K. J. J. *Oxygen Reduction and Carbon Monoxide Oxidation on Pt – from Model to Real Systems for Fuel Cell Electrocatalysis* PhD thesis, Vienna Univ. Technology (2005).

Author contributions Z.Z. and G.L. conceived the project and performed the computation. A.J.S., K.O., X.C., M.L. and I.T.M. performed the experiments. H.D., M.T.M.K., J.G. and Z.Z. supervised the project and provided the funding. Z.Z. wrote the manuscript. Z.Z., G.L., A.J.S., M.T.M.K. and J.G. revised the manuscript, and all authors contributed to the discussion and revision of the manuscript.
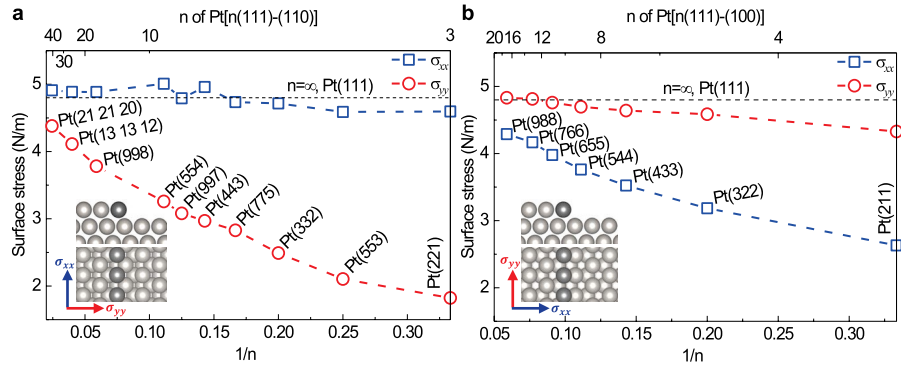
Extended Data Fig. 1 | Surface stress σ_{xx} and σ_{yy} of stepped Pt(111) surfaces with respect to the terrace width. Surface stress of Pt[n(111)-(110)] (a) and Pt[n(111)-(100)] (b) with respect to the terrace width n, and the inverse of terrace width, i.e. $1/n$, which corresponds to the step density. As a comparison surface stress of Pt(111) is also given. n is the number of atomic rows on the (111) terrace. The presence of steps leads surface stress release in the direction perpendicular to the step edges, which is in the y direction (σ_{yy}) for Pt[n(111)-(110)] and x direction (σ_{xx}) for Pt[n(111)-(100)], respectively. It is worth noting that surface stress release is proportional to the inverse of terrace width, i.e., step density.
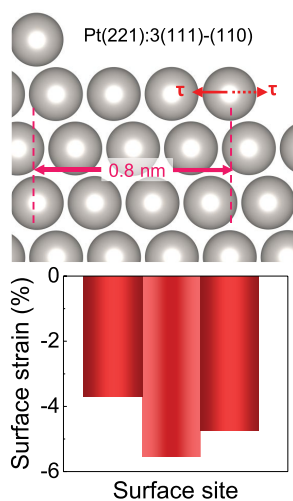
Extended Data Fig. 2 | Atomic site-resolved surface strain of Pt(221) surface with a terrace width of 0.8 nm ($n = 3$). Surface sites correspond to atoms in the top layer of the side view (upper panel). τ is intrinsic tensile surface stress, which is spontaneously released by introducing step to break symmetry, accompanied by the simultaneous generation of compressive surface strain. The terrace width is indicated by double arrow lines.
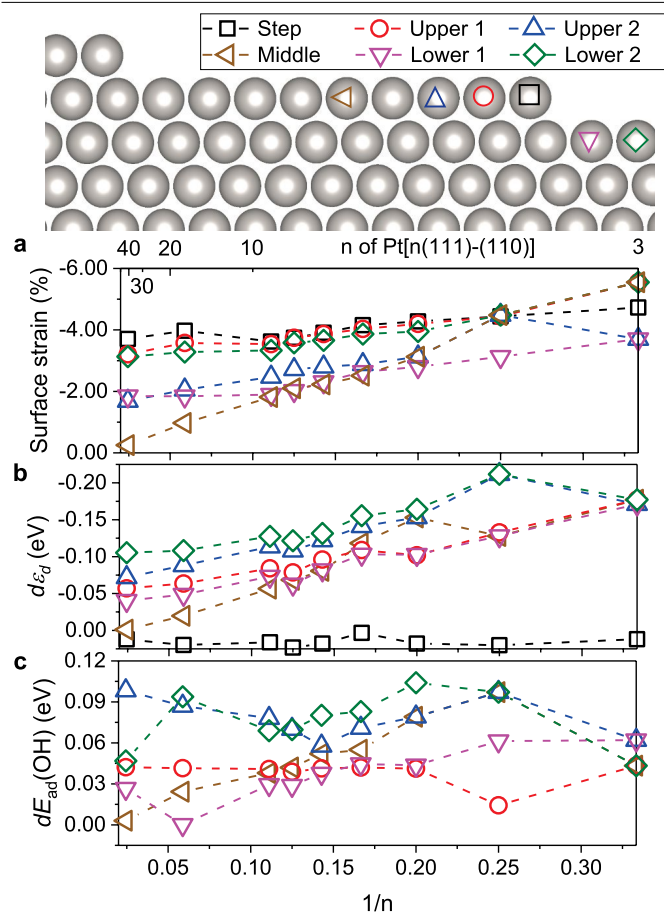
Extended Data Fig. 3 | Atomic site-resolved strain, electronic structure and surface reactivity as a function of the terrace width (_n_) and the inverse of terrace width (1/_n_), i.e., the step density. Shown are strain (a), _d_-band centre shift dε_d (b) and OH adsorption energy shift dE_{ad}(OH) (c) values, all evaluated with respect to that of Pt(111) for step edge atoms, atoms in the middle of terrace, and terrace atoms located immediately above (upper) and below (lower) the step edge, as indicated in the side view (upper panel).

Pt(221):3(111)-(110)

0.8 nm

a $d\varepsilon_d$ (eV)

b $dE_{ad}(OH)$ (eV)

c Improvement factor
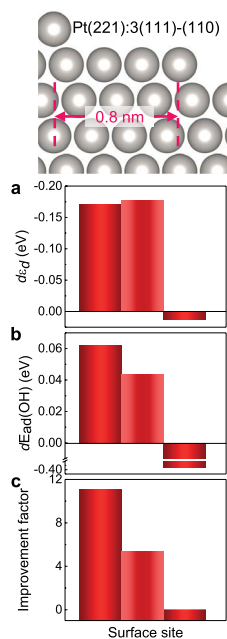
Surface site

Extended Data Fig. 4 | Atomic site-resolved electronic structure, surface reactivity and ORR activity of Pt(221) with respect to that of Pt(111) surface. Shown are d-band centre shift $d\varepsilon_d$ (a), OH adsorption energy shift $dE_{ad}(OH)$ (b), and ORR improvement factor (c). Surface sites correspond to atoms in the top layer of the side view (upper panel). The terrace width is indicated by double arrow lines.
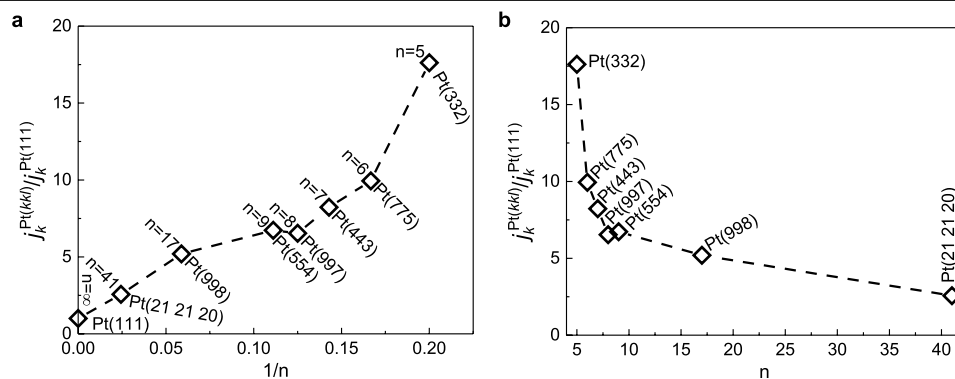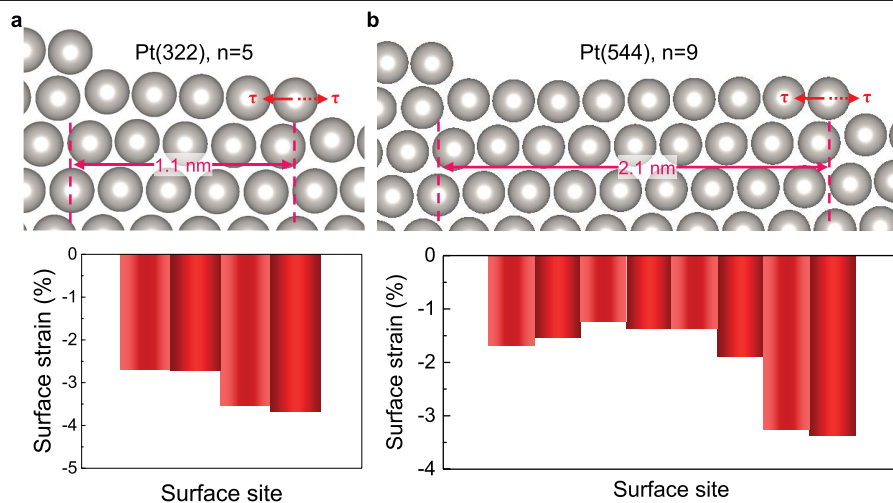
Extended Data Fig. 5 | The relationship between the predicted ORR activity enhancement and the terrace width *n* of Pt[*n*(111)-(110)]. (a) the enhancement factors (with respect to Pt(111)) versus the inverse of the terrace width, i.e. $1/n$, which corresponds to the step density, (b) the enhancement factors versus the terrace width *n*. It is worth noting that the main reason of showing enhancement factors versus step density is to compare with previous experiments[9,24,25].
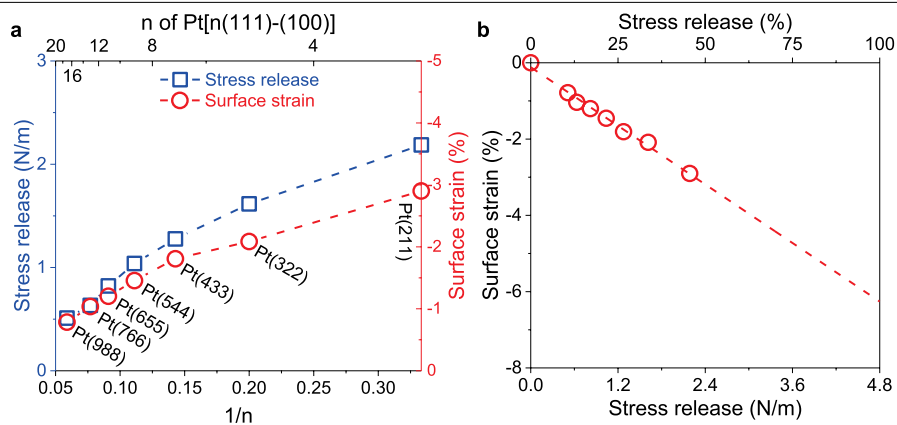
Extended Data Fig. 6 | Stress release and average surface strain of Pt[*n*(111)-(100)]. (a) Stress release and average strain as a function of the terrace width *n* and the inverse of terrace with, i.e., 1/*n*, which corresponds to the step density, (b) illustrating the linear relationship between the two parameters.

Extended Data Fig. 7 | Atomic site-resolved surface strain of Pt[n(111)-(100)] surfaces. (a) Pt(322) surface and (b) Pt(544) surface with a terrace width of 1.1 nm (n = 5) and 2.1 nm (n = 9), respectively. The terrace width is indicated by double arrow lines. Surface sites correspond to atoms in the top layer of the side views (upper panels). τ is intrinsic tensile surface stress, which is spontaneously released by introducing step to break symmetry, accompanied by the simultaneous generation of compressive surface strain.
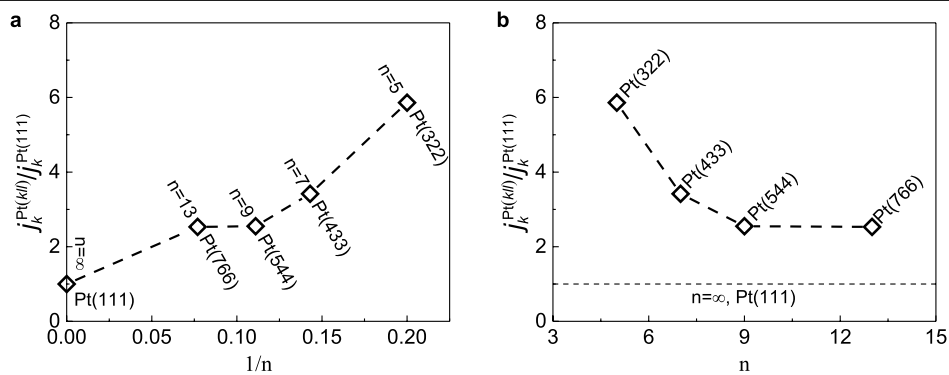
Extended Data Fig. 8 | The relationship between the predicted ORR activity enhancement and the terrace width n of Pt[n(111)-(100)]. (a) The enhancement factors (with respect to Pt(111)) versus the inverse of the terrace width, i.e., $1/n$, which corresponds to the step density, (b) the enhancement factors versus the terrace width n. It is worth noting that the main reason of showing enhancement factors versus step density is to compare with previous experiments[9,24].
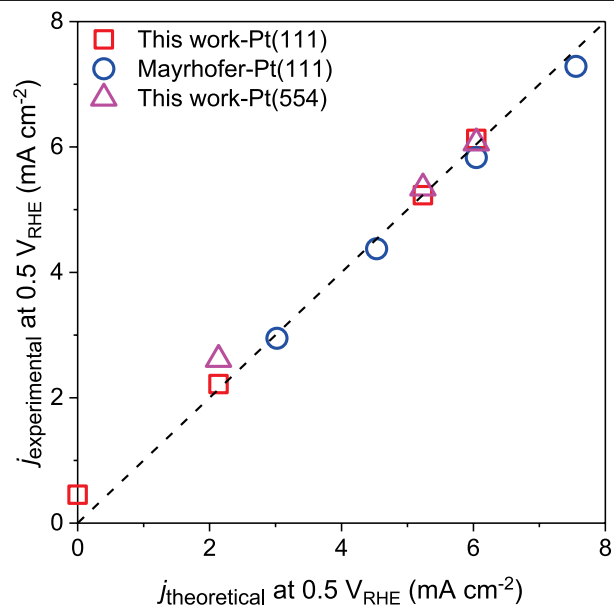
Extended Data Fig. 9 | Experimentally measured ORR limiting current as a function of predicted ORR limiting current. Experimental data for ORR on Pt(111) are taken from ref. 53; and for ORR on Pt(111) and Pt(554) from this work. ORR reaction conditions: O_2-saturated 0.1 M $HClO_4$ at 23 °C at 0.5 V_{RHE} with a scan rate of 10 mV s^{-1} and varying rotation rates.
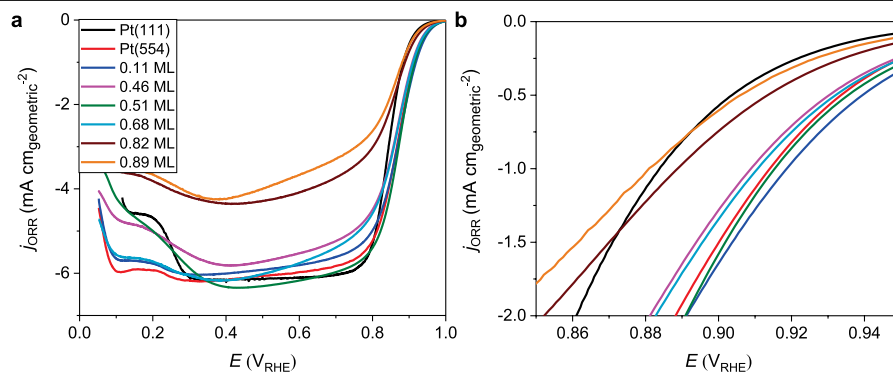
Extended Data Fig. 10 | ORR polarization curves for Pt(554) surface with 0 ML to 0.9 ML Au deposited at the step edge. (a) The full polarization curves in the potential region from 0.05 to 1 V_{RHE}. (b) The polarization curves in the potential region from 0.85 to 0.95 V_{RHE}.

Extended Data Table 1 | Calculated surface stress of n(111)-(110) and n(111)-(100) stepped surfaces with different terrace width n

Pt(kkl), n(111)-(110)		Surface stress (N/m)		Pt(kll), n(111)-(100)		Surface stress (N/m)	
Pt(kkl)	n	σ_{xx}	σ_{yy}	Pt(kll)	n	σ_{xx}	σ_{yy}
Pt(221)	3	4.60	1.82	Pt(211)	3	2.63	4.33
Pt(553)	4	4.59	2.10	Pt(322)	5	3.18	4.59
Pt(332)	5	4.72	2.49	Pt(433)	7	3.52	4.64
Pt(775)	6	4.74	2.83	Pt(544)	9	3.76	4.70
Pt(443)	7	4.96	2.97	Pt(655)	11	3.98	4.76
Pt(997)	8	4.79	3.08	Pt(766)	13	4.17	4.81
Pt(554)	9	5.01	3.26	Pt(988)	17	4.29	4.83
Pt(998)	17	4.89	3.78	Pt(111)	∞	4.80	4.80
Pt(13 13 12)	25	4.89	4.11				
Pt(21 21 20)	41	4.91	4.38				
Pt(111)	∞	4.80	4.80				

n is the number of atomic row on (111) terraces.

Extended Data Table 2 | Thermodynamic data used in the free energy analysis

	ZPE (eV)	δH (eV)	TS@298K (eV)	E_{sol} (eV)	$E_{correction}$ (eV)
H_2O	0.56	0.10	0.68		
H_2	0.27	0.09	0.41		
OOH*	0.44	0.05		-0.40	0.07
O*	0.04	0.02			0.37
OH*	0.34	0.03		-0.56	0.12